Journal of Solid State Chemistry 184 (2011) 2066–2074

Contents lists available at ScienceDirect

Journal of Solid State Chemistry

journal homepage: www.elsevier.com/locate/jssc

Effects of quartz particle size and water-to-solid ratio on hydrothermal synthesis of tobermorite studied by in-situ time-resolved X-ray diffraction

J. Kikuma [a,*], M. Tsunashima [a], T. Ishikawa [a], S. Matsuno [a], A. Ogawa [b], K. Matsui [b], M. Sato [c]

[a] Analysis and Simulation Center, Asahi-KASEI Corporation, 2-1 Samejima Fuji, Shizuoka 416-8501, Japan
[b] Construction Materials Laboratory, Asahi-KASEI Construction Materials Corporation, Sakai-machi, Ibaraki 306-0493, Japan
[c] Industrial Application Division, SPring-8/JASRI, Sayo, Hyogo 679-5198, Japan

ARTICLE INFO

Article history:
Received 3 November 2010
Received in revised form
17 February 2011
Accepted 30 May 2011
Available online 13 June 2011

Keywords:
Tobermorite
In-situ
X-ray diffraction
Hydration
Autoclave

ABSTRACT

Hydrothermal synthesis process of tobermorite ($5CaO \cdot 6SiO_2 \cdot 5H_2O$) has been investigated by in-situ X-ray diffraction using high-energy X-rays from a synchrotron radiation source in combination with a purpose-build autoclave cell. Dissolution rates of quartz were largely affected by its particle size distribution in the starting mixtures. However, the composition (Ca/Si) of non-crystalline C–S–H at the start of tobermorite formation was identical regardless of the quartz dissolution rate. An effect of water-to-solid ratio (w/s) was investigated for samples using fine particle quartz. Tobermorite did not occur with w/s of 1.7 but occurred with w/s higher than 3.0. Surprisingly, however, the dissolution curves of quartz were nearly identical for all samples with w/s from 1.7 to 9, indicating that the dissolution rate is predominated by surface area. Possible reaction mechanism for tobermorite formation will be discussed in terms of Ca and/or silicate ion concentration in the liquid phase and distribution of Ca/Si in non-crystalline C–S–H.

1. Introduction

Tobermorite is one of the most industrially important calcium silicate hydrates because it is a major constituent in autoclaved aerated concrete (AAC), which is widely used as a building material [1,2]. A typical process for the AAC production includes hydrothermal treatment of a mixture of quartz sand, lime, cement and gypsum at high temperatures (typically, 180–200 °C) under a saturated steam pressure. It has been reported that both quantity and quality of tobermorite formed in the AAC significantly affect its mechanical properties [3,4]. Thus, understanding of the mechanism of tobermorite formation is important if improvement of properties of AAC is to be achieved.

The synthesis of tobermorite under hydrothermal conditions has been extensively studied, mainly using ex-situ approaches, in which the samples were taken out from the autoclave at various stages of the reaction. Hydrothermal syntheses using various starting materials including several types of silica sources [5–13], in combination with reactive Al compounds [14–23], have been reported.

However, such ex-situ approaches include ambiguity caused by the temperature dependence of solubility, unfavorable reactions during the cooling process, variation among different pieces used as samples at different reaction stages, and so on.

Thus, an in-situ approach is more desirable for understanding the reaction in detail. Several in-situ approaches have been reported for monitoring hydrothermal reactions by means of transmission X-ray diffraction (XRD) [24–30] and transmission energy-dispersive XRD [30–35]. Most of the reaction cells used in these studies were quite small, for example, capillary tubes or metal thin pipes, because such small cells make pressure sealing easier. However, the accuracy of the temperature and the pressure control in the cell would not be sufficient because direct monitoring of these parameters is difficult inside small cells. It is also difficult to precisely control the water-to-solid ratio (w/s) in such small cells, even though it is one of the most important parameters in hydrothermal reaction.

Recently, we have developed a relatively large-sized in-situ XRD cell for autoclave reaction, and successfully observed the AAC production process with high precision [36–38]. Samples investigated in our previous studies were those close to the real industrial AAC production, which include cement as starting materials. It has been revealed that several intermediate phases, including Al or S from the cement, play important roles for tobermorite formation [37,38]. However, cement includes a certain amount of impurities and tends to have a wide variation in particle size. In fact, in our previous studies, very strong diffraction spots from large single crystals of quartz and portlandite originating from the cement were occasionally observed, and these made quantitative discussions difficult.

In the present study, starting materials without cement were utilized for investigating the hydrothermal formation of tobermorite

* Corresponding author. Fax: +81 545 62 3189.
E-mail address: kikuma.jb@om.asahi-kasei.co.jp (J. Kikuma).

0022-4596/$ - see front matter © 2011 Elsevier Inc. All rights reserved.
doi:10.1016/j.jssc.2011.05.061

in more quantitative manner. Quartz sand whose particle size distributions are well defined and research grade CaO were used as starting materials. In addition, a large-sized pixel array detector for transmission XRD (24 times larger than that used in the previous study) was utilized to improve the statistics.

2. Experimental

2.1. Materials and sample preparation

The starting materials were mixtures of 56 wt% natural quartz sand (purity > 99.4%) and 44 wt% quicklime (CaO: 99.9%, Kanto Kagaku), which had been carefully sealed and stored to avoid hydration during the storage. The weight increase of quicklime by hydration during the weighing and handling was less than 0.05% of the total amount of quicklime. The molar ratio of Ca/Si in these mixtures was 0.84, which is nearly identical to stoichiometric value of tobermorite. Three types of quartz sand having different particle size distributions were used; average particle size of 2.2 μ (denoted as "fine"), 4.2 μ ("medium") and 25 μ ("coarse").

The starting mixtures were fully mixed in the presence of water at 50 °C for several minutes using a motor-driven blade stirrer. The w/s was 1.5 or 1.7 by weight, except for the mixtures with the fine quartz sand, for which the slurry with the w/s of 1.7, 3.0, 6.0 and 9.0 were prepared. The list of samples is shown in Table 1. For each run, the slurry was poured into a plastic beaker, sealed in a plastic bag and kept at 50 °C for more than 8 h for the quicklime in the mixture to become hydrated. The hydrated slurry was then cooled down, and poured into a sample holder of 3.0 mm sample thickness.

2.2. In-situ XRD measurement

A schematic of the experimental set-up is presented in Fig. 1. A slurry sample was set in the originally made autoclave cell for in-situ transmission XRD measurement. Details of the autoclave cell are described elsewhere [36–38]. Briefly, the autoclave cell is made of stainless steel, and consists of a rectangular parallelepiped main body (capacity: 35 cm^3) and a lid. The cell has two beryllium windows welded on the center of the side walls for both incoming and diffracted X-rays. The temperature and pressure inside the cell can be monitored directly using the sensors inserted into the cell. The bottom part of the cell was filled with 5 cm^3 of distilled water. The sample holder was set in the center position of the cell using a mounting stand so that the sample slurry did not make contact with the water directly. The temperature of the cell is controlled by a copper heater block surrounded by a heat insulator. The steam temperature is measured a few millimeters away from the sample. Both the temperature and the pressure were very stable throughout the experiment. The pressure at 190 °C was close enough to the value of the saturated steam pressure with a slight error corresponding to a few degree of temperature difference.

Table 1
List of samples for in-situ XRD.

Sample	Quartz particle size	w/s	Autoclave time (h)
M-1.7	Medium	1.7	10.5
M-1.5	Medium	1.5	10.5
C-1.5	Coarse	1.5	13.5
F-1.7	Fine	1.7	6.3
F-3	Fine	3.0	10.5
F-6	Fine	6.0	10.5
F-9	Fine	9.0	10.5

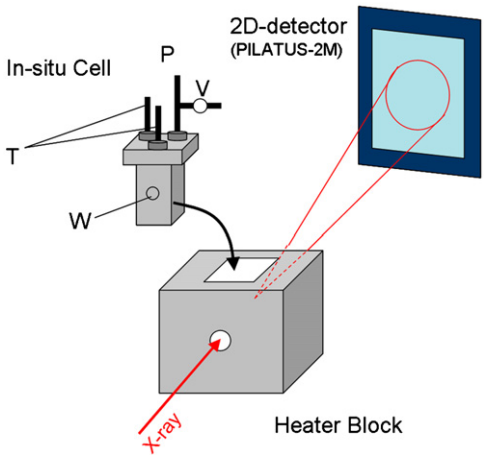

Fig. 1. Schematic of the experimental set-up. T: temperature sensors, P: pressure sensor, V: pressure release valve and W: Be window.

In-situ XRD measurements were carried out at the BL19B2 beamline of SPring-8, using an X-ray energy of 30 keV. The X-ray beam size was set to be 0.8 mm wide and 0.12 mm high. The autoclave cell with a sample and water inside was set in the copper heater block. First, the temperature was elevated to 100 °C at a heating rate of 2 °C/min. The temperature was held at 100 °C for 15 min. During this period, the air inside the cell was removed by opening a pressure release valve for a few seconds. After the steam pressure was built up again at 100 °C, the first XRD measurement was conducted. After 15 min at 100 °C, the temperature was elevated again to 190 °C at a heating rate of 1 °C/min, and then held at 190 °C for typically 9 h. During this process, the XRD measurements were conducted using a photon-counting pixel array detector with the pixel size of 172 μ, PILATUS-2M (DECTRIS).

The PILATUS-2M detector was placed downstream at a sample-to-detector distance of about 800 mm. The sample-to-detector distance in each experiment was calibrated using quartz peak positions. Typical exposure time for one image was 2.0 min, and the measurement interval was 3.0 min. For higher w/s samples (F-6 and F-9), the exposure time and the measurement interval were 4.0 and 5.1 min, respectively. During the exposure time, the cell, together with the heater block, was oscillated in the vertical direction by 3.0 mm at a rate of 0.6 mm/s to average over larger area of the sample. For each sample, about 200 measurement cycles were conducted during the typical autoclaving time of 10.5 h (see Table 1). Circular diffraction patterns were obtained for a diffraction angle range (2θ) of 0.5–14.0°, which corresponds to 2–55° for that of Cu$K\alpha$ X-ray source. An example of image data obtained by the PILATUS-2M detector is shown in Fig. 2. The white grid-lines in Fig. 2 are the gap between two modules, as the PILATUS-2M consists of 24 smaller PILATUS modules.

2.3. Data analysis

It is common to calculate circular average of two-dimensional data to obtain one-dimensional diffraction patterns. In the present study, however, horizontal part of the circular signal was broadened because the incident beam was long, rectangular in shape along the horizontal direction. Thus, only upper part of the circular signal (from −45 to 45°) was taken for sector average to obtain one-dimensional diffraction patterns, as shown in Fig. 2. The sector average was calculated by Igor Pro software (HULINKS) using macro-procedures. Peak intensities were determined by peak areas after entire diffraction patterns being normalized with the transmitted beam intensities, in order to correct the change of incident beam intensity. The peak area for each reflection was

determined by numerical integration after baseline subtracted. For the intensity of C–S–H halo, baseline was drawn for wide 2θ range, 7.34–9.23°, and the intensity for the 2θ range of 7.81–7.85° above the baseline was integrated. Peak positions of tobermorite were determined by the middle point of two half-maximum positions, which were calculated from the interpolation of the nearest two data points. The tobermorite peak positions were calibrated using quartz peak positions.

The reaction times shown on the horizontal axes of the figures are defined as the times at the beginning of the corresponding measurement cycle, and the time zero is defined as the time at which the temperature started to be elevated from 100 to 190 °C.

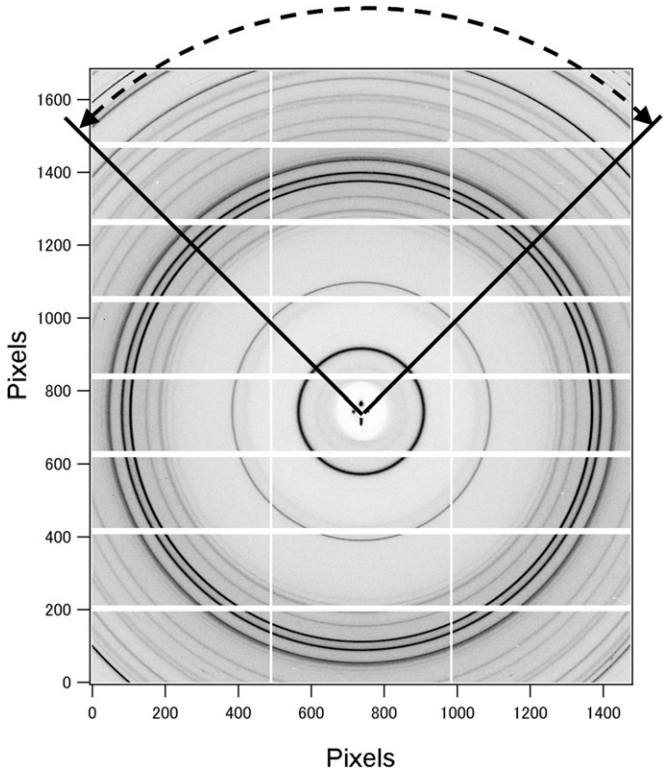

Fig. 2. Typical XRD image acquired using a PILATUS-2M detector. The range of the sector average to obtain one-dimensional diffraction patterns is indicated. The white grid-lines in the figure are the gap between two modules, as a PILATUS-2M consists of 24 smaller PILATUS modules.

3. Results and discussion

3.1. Phase evolution—typical in-situ XRD data

Fig. 3 shows the time-resolved XRD data set for sample M-1.7 under autoclave condition up to 300 min. The phase evolution during the autoclave is quite simple in this sample. At the beginning of the autoclave (at 100 °C), quartz and portlandite ($Ca(OH)_2$) were observed. Quicklime was fully hydrated to portlandite during the pre-curing process at 50 °C and not observed in the in-situ XRD data. Portlandite first decreased and disappeared at about 100 min, while quartz started to decrease a little later than portlandite. As the dissolutions of both materials proceed, amorphous halo originating from non-crystalline C–S–H was clearly observed. Then, at around 120 min (30 min after the temperature reached 190 °C), tobermorite peaks started to be observed. Tobermorite intensity became nearly saturated after 300 min, as will be described in the next section. This type of data set was obtained for all samples in Table 1, and peak intensities were determined for each constituent.

3.2. Effect of quartz particle size

Three types of quartz having different particle size distribution were used as starting materials with slightly different w/s ratios. In this section, results for samples M-1.7, M-1.5, C-1.5 and F-1.7 will be discussed.

Before we describe the in-situ data, we would like to compare the data of last measurement cycle of each sample to show how the final products are different from each other. Fig. 4 shows XRD data of the last measurement cycle for each sample. Both M-1.7 and M-1.5 showed typical tobermorite patterns, and nearly identical to each

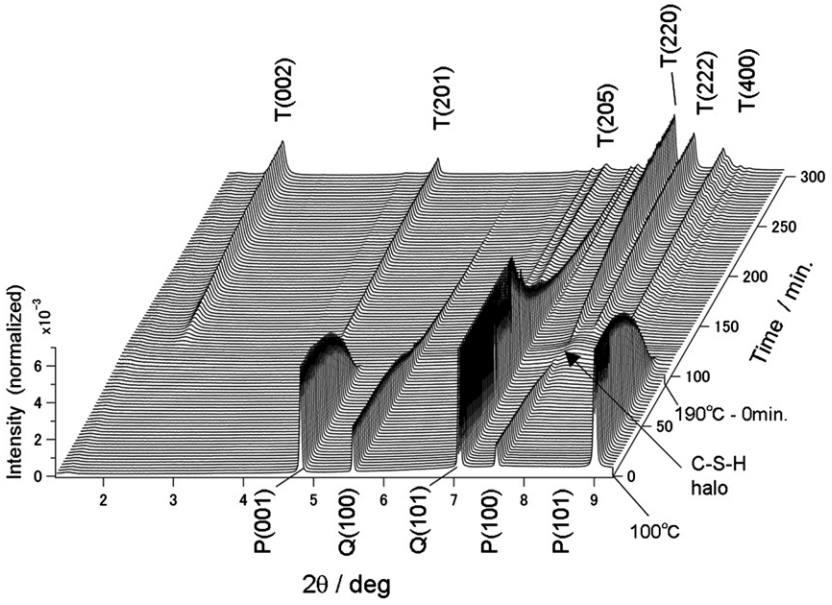

Fig. 3. Stack of time-resolved XRD patterns for sample M-1.7. Temperature was elevated from 100 to 190 °C and then held at 190 °C . T: tobermorite, P: portlandite and Q: quartz. Vertical scale is expanded so that tobermorite peaks can be clearly recognized. Thus, initial part of Q(101) intensity is out of scale.

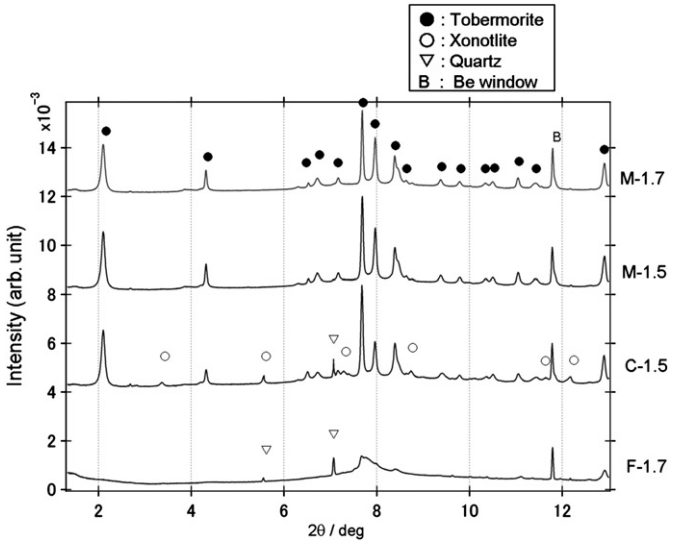

Fig. 4. XRD patterns of the final measurement cycle in in-situ experiment for samples using quartz having different particle size distribution (see text and Table 1 for detailed sample information).

other, indicating that, as far as final products are concerned, the hydrothermal reaction is not largely affected by the slight w/s difference from 1.7 to 1.5. Sample C-1.5 showed different XRD patterns from those of M-1.7 and M-1.5. In addition to tobermorite (T), xonotlite (Xo: $6CaO \cdot 6SiO_2 \cdot H_2O$) peaks were clearly observed. It should also be noted that the intensity ratio of T(002) (at 2.10°) and T(222) (at 7.97°) is obviously different from those of M-1.7 and M-1.5, as will be discussed later. Sample F-1.7 showed totally different XRD pattern from other samples. Neither tobermorite nor xonotlite peak was observed. Instead, a typical pattern of semi-crystalline C–S–H [39] was observed around 7.7°. Note that, in this paper, the term "semi-crystalline C–S–H" has different meaning from "non-crystalline C–S–H." "Semi-crystalline C–S–H" is a type of C–S–H that shows broad peaks in XRD pattern [39–41], while "non-crystalline C–S–H" is a type of C–S–H that does not show any peaks and only shows amorphous halo and is typically observed in the middle of synthesis process of tobermorite [6,42].

The time dependencies of the intensities of major peaks of M-1.7 in in-situ XRD are plotted in Fig. 5(a) and (b). In Fig. 5(a), the intensities of 4 peaks from quartz (Q) and 2 peaks from portlandite (P) are plotted together. In Fig. 5(b), 5 peaks from tobermorite (T) are plotted. In addition, intensity of non-crystalline C–S–H halo is plotted, which is defined as the intensity at 7.83° after baseline subtracted (see Section 2). Fig. 5(c) shows normalized peak intensities of quartz, portlandite and tobermorite. For tobermorite, the intensities are normalized to the intensity at 300 min. Although all of the time-dependence curves from the same constituents are nearly identical to each other, the Q(112) curve showed a slight 'tailing' in the late stage of the autoclave. This was due to the overlap of tobermorite (603) peak, which appears at almost the same 2θ position. Thus, the tailing should not be regarded as a real quantity of the quartz, although the initial part of the curve is considered to be accurate.

A similar result was obtained for sample M-1.5, confirming that the difference in w/s of 1.7 and 1.5 does not affect the reaction very much, except that the formation rate of tobermorite was a little bit slower, as is shown in Fig. 9.

The time dependencies of the peak intensity data for sample C-1.5 are plotted in Fig. 6(a) and (b), together with the normalized data, Fig. 6(c), in which tobermorite peaks are normalized by the intensity at 500 min to be 0.667. The total autoclave time for this sample was longer than others. It is shown that the overall

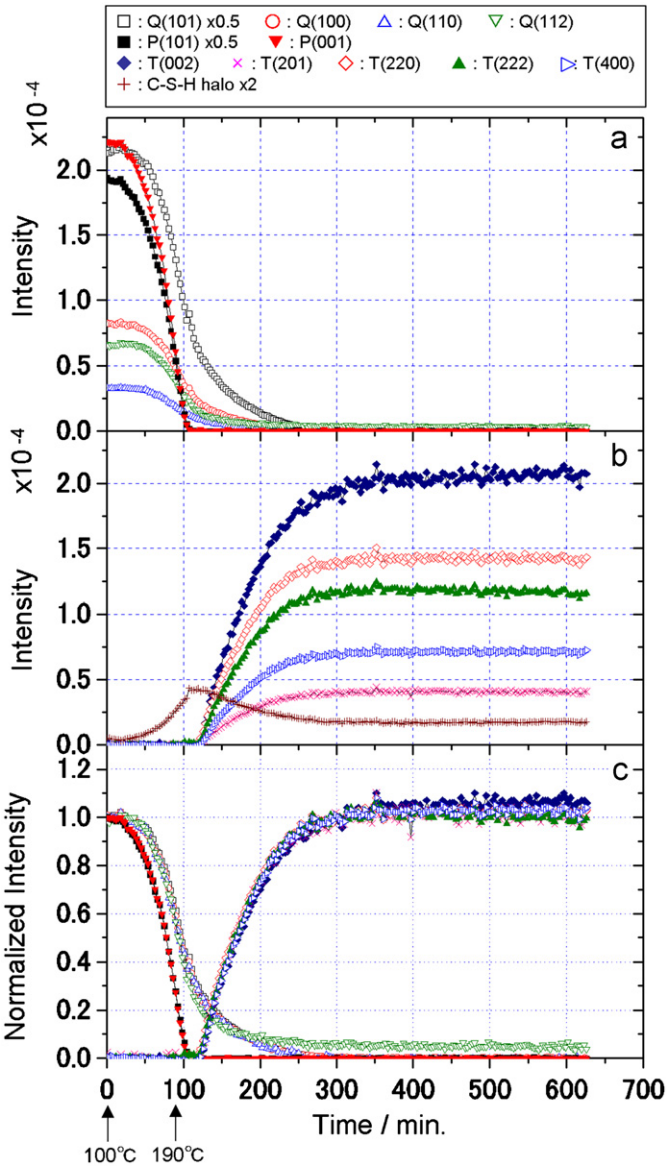

Fig. 5. Time dependence of peak intensities for the major constituents in sample M-1.7: (a) raw data for portlandite and quartz, (b) raw data for tobermorite and non-crystalline C–S–H and (c) normalized data. T: tobermorite, P: portlandite and Q: quartz.

reaction was much slower than that of M-1.7 owing to the larger particle size of quartz. It should be noted that not only the dissolution rate of quartz but also that of portlandite significantly decreased, indicating that the dissolutions of quartz and portlandite are closely associated with each other. This may be attributed to high Ca^{2+} ion concentration in the solution phase. In our previous study, in which samples including cements were used, Ca^{2+} ion concentration was considered to be nearly saturated with respect to portlandite at the beginning of the autoclave [37,43]. Thus, portlandite cannot be dissolved further unless Ca^{2+} ions in the solution phase are consumed in some way, that is, by the formation of non-crystalline C–S–H. Similar phenomena would occur in the present study. The time dependence of non-crystalline C–S–H halo is also consistent with this phenomenon.

In addition to tobermorite, xonotlite (Xo) was formed in C-1.5. In Fig. 6(b), time dependence of Xo(001) peak intensity is plotted together. Xonotlite started to be observed at around 500 min and increased to the end of the autoclave. It should be noted that the total autoclave time is longer for C-1.5; however, when compared

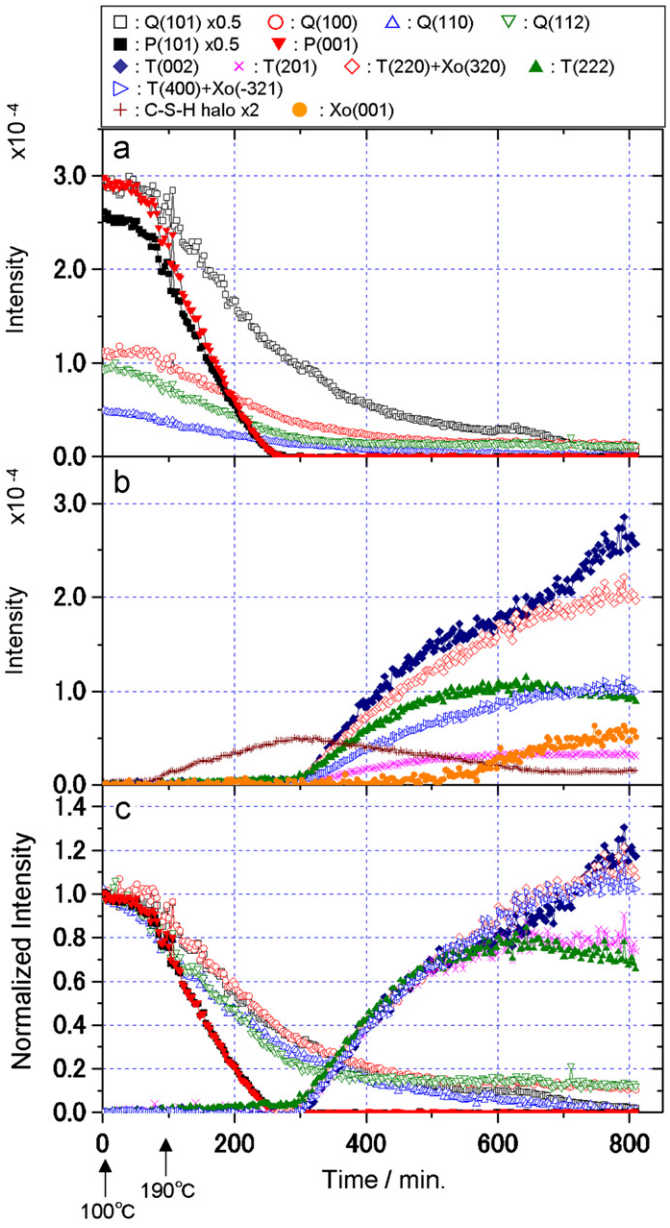

Fig. 6. Time dependence of peak intensities for the major constituents in sample C-1.5: (a) raw data for portlandite and quartz, (b) raw data for tobermorite, xonotlite and non-crystalline C–S–H, and (c) normalized data. T: tobermorite, P: portlandite, Q: quartz and Xo: xonotlite.

at the same autoclave time as M-1.7 or M-1.5, xonotlite formation is clearly observed in C-1.5. It has been reported that hydrothermally synthesized tobermorite decomposes into xonotlite in a certain autoclave condition with a long processing time over 10 h [8,44]. According to the literature, the tobermorite decomposition is likely to occur when quartz with coarse particle size (10–20μ) is used as a starting material, although the reason for this is not clear. The result in this work is basically consistent with those in the literature. One possible reason for xonotlite formation is high Ca/Si ratio in non-crystalline C–S–H during the autoclave. In C-1.5, the dissolution rate of quartz is very low even after the tobermorite formation. Thus, Ca/Si value in non-crystalline C–S–H remains high for a long time at 190 °C (see Fig. 10 for detail). This may increase the possibility of xonotlite formation compared to other samples. It is possible to consider the change in tobermorite phase in more detail by looking into the intensity change of tobermorite peaks. In Fig. 6, changes of the tobermorite peak intensities after the xonotlite formation are clearly observed. Note that some of the tobermorite peaks overlap with xonotlite peaks, namely, T(220) and Xo(320) and T(400) and Xo(−321). Thus we exclude these tobermorite peaks from the discussion of intensity change along with xonotlite formation. T(201) intensity seems nearly saturated, and T(222) intensity is decreased at the late stage of the autoclave. The decrease of tobermorite peak would indicate the decomposition of tobermorite, and decomposed tobermorite would become a source of xonotlite. T(002) intensity, on the other hand, increased more rapidly at the late stage of the autoclave.

The reason for the increase of T(002) peak intensity in C-1.5 after 650 min should be considered. Texture change during the reaction is unlikely to occur because the sample is in slurry form at the beginning of the autoclave and transmission geometry was used for the XRD measurement. To consider the possibility of chemical composition or structure change in sample C-1.5, the tobermorite peak positions during the reaction are shown in Fig. 7. For T(002), T(400) and T(201), peak shifts were observed after 650 min. The observed peak shifts correspond to the *d*-spacing decrease by 0.3% and 0.1% for *c* and *a* axes, respectively. Judging from the fact that the intensity change of T(002) and peak shifts of three tobermorite peaks started at the same time, it is reasonable to consider that the intensity change and the peak shift are related to each other. As described above, the amount of *d*-spacing changes of tobermorite after 650 min are small, while the T(002) intensity change after 650 min is quite significant. Thus, not only the *d*-spacing changes but also the chemical composition change might have occurred. Tobermorite crystal has a layered structure with Ca atoms and water molecules at the interlayer region. The amounts of these interlayer atoms/molecules can be changed without significant change of crystal

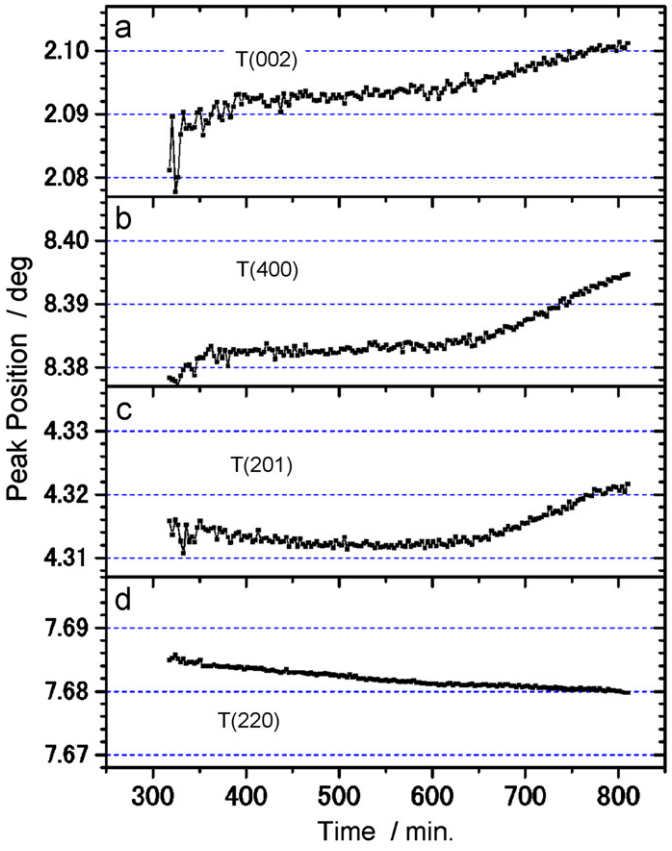

Fig. 7. Time dependencies of tobermorite peak positions in sample C-1.5. (a) T(002), (b) T(400), (c) T(201) and (d) T(220).

framework [45–47]. Thus, one possible reason for the T(002) intensity change with a slight decrease of the *c*-axis length would be the decrease of interlayer Ca atoms or water molecules. During the intensity change, xonotlite kept increasing in the system. As Ca/Si for xonotlite is larger than that of tobermorite, the formation of xonotlite requires more Ca from the system. This would lead to the ejection of Ca from tobermorite. Preliminary calculation of XRD pattern for various site occupancy factors of interlayer Ca atom and water molecule was conducted by a crystal structure analysis software (Materials Studio: Accelrys) using a tobermorite crystal structure from ICSD database as an input file. The decrease of the interlayer Ca atom and water molecule both resulted in the intensity increase of T(002), and the increase of relative intensity against other peaks, which qualitatively supports the hypothesis. (The results are shown in supplemental figures.)

The precise structural refinement by powder pattern simulation such as Rietveld analysis will be necessary for further discussion.

The time dependencies of the peak intensities for sample F-1.7 are plotted in Fig. 8(a), together with the normalized data, Fig. 8(b). No tobermorite peak was observed in F-1.7, thus not plotted in Fig. 8(a). Instead, semi-crystalline C–S–H was observed. It is not surprising that no tobermorite was formed in F-1.7, because a number of past studies have already shown the difficulty of synthesizing tobermorite from a highly reactive silica source [6–8,10,12]. The peak intensity of semi-crystalline C–S–H (broad peak at 7.7°) is plotted together in Fig. 8(b), which is defined as the same 2θ range as T(220). Note that there is no tobermorite observed in sample F-1.7, and the intensity profile of semi-crystalline C–S–H in Fig. 8(b) is not distorted by the T(220) signal. It is shown that semi-crystalline C–S–H started to be observed immediately after portlandite was completely dissolved.

In order to compare the results of different samples, normalized curves from the same constituents were averaged to obtain better statistics (For example, 5 tobermorite curves in Fig. 5(c) were averaged to obtain one tobermorite curve. The same for quartz and portlandite.). The averaged results for M-1.7, M-1.5, C-1.5 and F-1.7 are plotted in Fig. 9. For quartz, Q(112) data was excluded from the average data for the reason described above. For C-1.5, even though some of the tobermorite peaks overlap with those of xonotlite, all 5 peaks were averaged to discuss only the early stage of tobermorite formation. For F-1.7, the intensity of semi-crystalline C–S–H, instead of tobermorite, was plotted. It is clearly shown that the dissolution rates of quartz and portlandite decrease with increase in quartz particle size. For all samples, portlandite is completely dissolved just

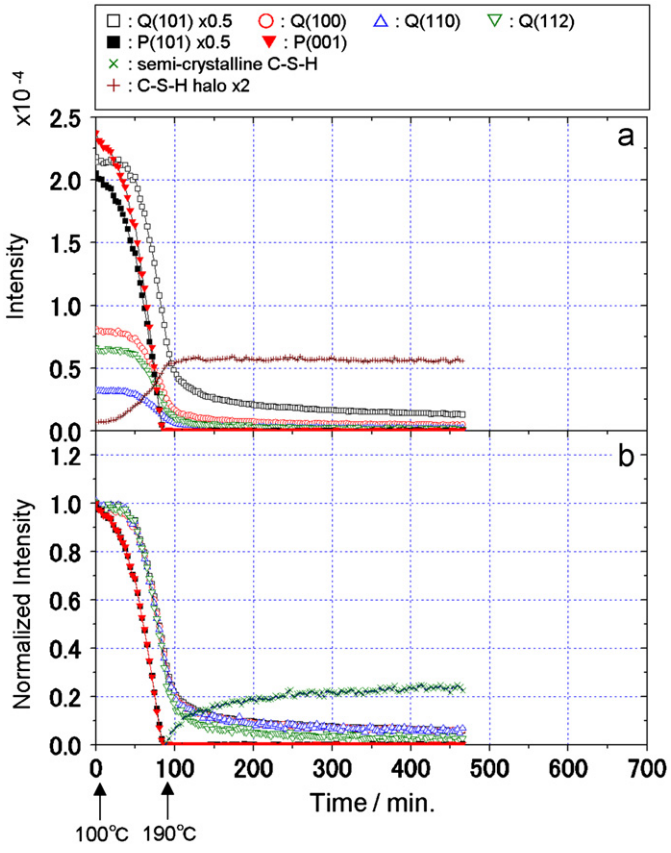

Fig. 8. Time dependence of peak intensities for the major constituents in sample F-1.7: (a) raw data and (b) normalized data. P: portlandite and Q: quartz.

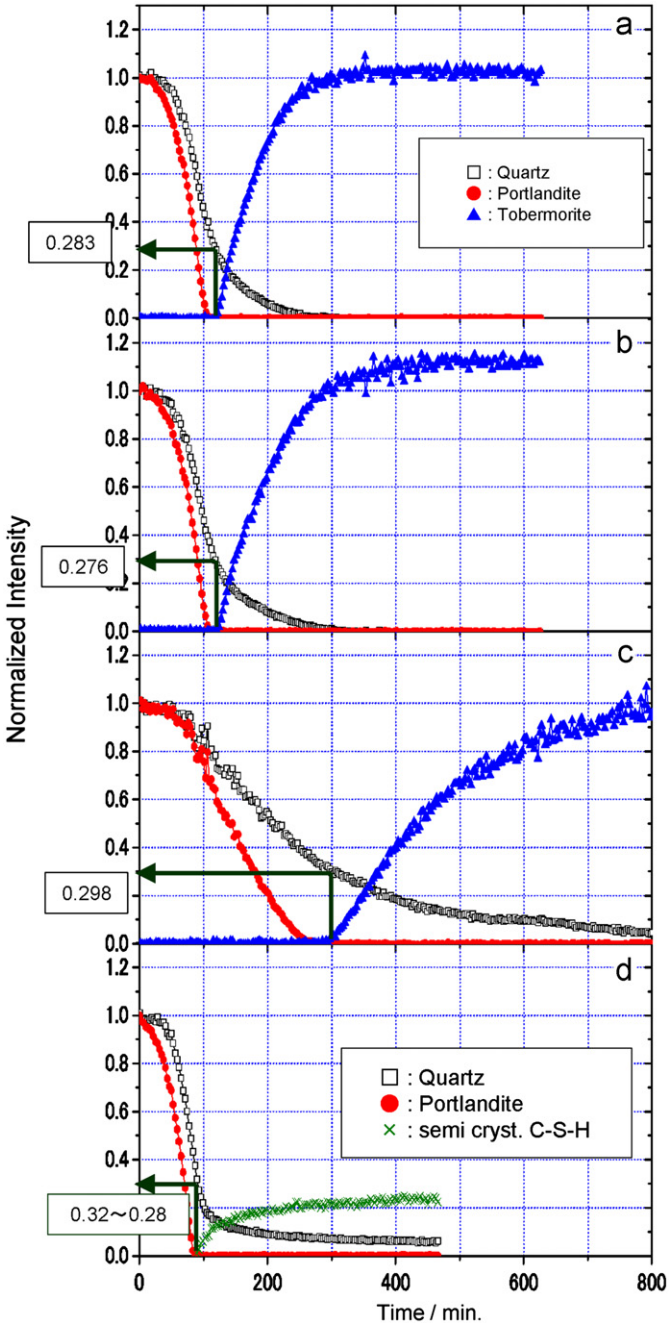

Fig. 9. Time dependence of the averaged peak intensities of the major constituents for (a) M-1.7, (b) M-1.5, (c) C-1.5 and (d) F-1.7.

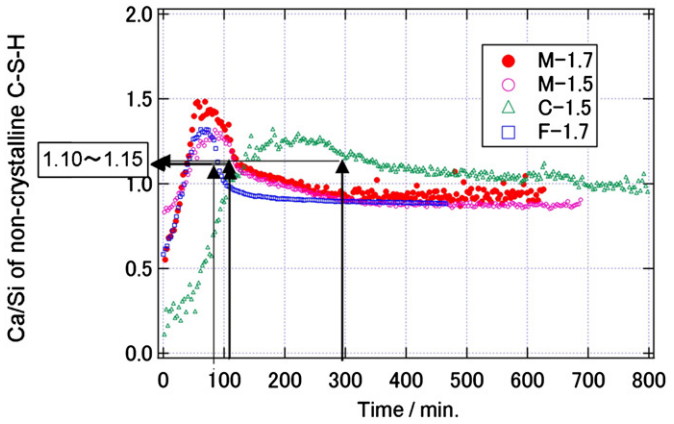

Fig. 10. Time dependence of calculated Ca/Si ratios in non-crystalline C–S–H. Vertical arrows indicate the time at which either tobermorite or semi-crystalline C–S–H starts to be observed.

before either tobermorite or semi-crystalline C–S–H started to be formed, while a certain amount of quartz remained undissolved. The amount of residual quartz at that time that either tobermorite or semi-crystalline C–S–H started to be formed (hereafter, denoted by T0) is shown for each sample in Fig. 9. It is interesting that the amount of the remaining quartz at T0 is nearly identical for all samples regardless of the absolute value of T0. This suggests that the non-crystalline C–S–H starts to be transformed to either tobermorite or semi-crystalline C–S–H at a certain composition threshold. The time dependence of the Ca/Si value of non-crystalline C–S–H can be calculated from the in-situ XRD peak intensities of quartz and portlandite, assuming that all of the dissolved quartz and portlandite are incorporated in non-crystalline C–S–H [48,49]. The amounts of quartz and portlandite remaining in the system were determined by peak intensity relative to those for starting mixture before autoclave. The amounts of quartz and portlandite in the starting mixture were determined by laboratory XRD intensity relative to those of a model mixture of dry quartz and portlandite powder. The calculated Ca/Si values of non-crystalline C–S–H are plotted in Fig. 10. The Ca/Si ratio of non-crystalline C–S–H becomes higher at about several tens of minutes before T0, and then decreases. The transformation to either tobermorite or semi-crystalline C–S–H is expected to occur at the non-crystalline C–S–H composition below a certain Ca/Si value, about 1.13. It should be noted that Ca/Si curve of C-1.5 remains above 1.0 for a few hundreds of minutes after the beginning of tobermorite formation, which may be a cause of xonotlite formation as described above.

The Ca/Si values at T0 for samples with different quartz particle size are nearly identical to each other. This result is somewhat contradictory to the mechanism presented in earlier studies. It has been stated that the reason for the difficulty of synthesizing tobermorite from highly reactive silica is that the silica dissolves so fast that the Ca/Si of non-crystalline C–S–H tends to be low from the beginning, and it has been considered to be difficult for the non-crystalline C–S–H having low Ca/Si to be transformed to tobermorite [6,12,16]. In the present study, however, the Ca/Si of non-crystalline C–S–H at T0 is not different among different quartz size samples. In other words, for the sample containing fine quartz (F-1.7), tobermorite cannot be formed even when the Ca/Si value is high enough at about 190 °C. Therefore, we assume there are some other parameters that determine whether tobermorite can be formed or not. One possibility is the structure of non-crystalline C–S–H, more specifically, silicate chain length in non-crystalline C–S–H. According to the NMR analysis by Sato and Grutzeck [6], C–S–H with Ca/Si >1, which has short silicate chains, is likely to be rearranged and transformed to tobermorite, while C–S–H with Ca/Si <1, which has long and/or cross-linked silicate chains is not. It is of interest to investigate the silicate chain length for samples in the present study. Another possibility is the distribution of the Ca/Si within non-crystalline C–S–H. Even the average Ca/Si values of C–S–H are identical among these samples, but their distribution may be different. Let us consider the relationship between the Ca/Si distribution and the particle size of quartz. When fine particle quartz is used, a large number of quartz particles are spread over the system with short particle-to-particle distance. If large particles are used, a small number of the quartz particles exist with longer distance. Considering that they start to be dissolved to form non-crystalline C–S–H, the spatial gradient of silicate ion concentration would be different according to the quartz particle size. This might lead to the difference in non-uniformity of Ca/Si in non-crystalline C–S–H, and to the difference in possibility of the transformation to tobermorite. Investigations of silicate chain length and Ca/Si distribution in non-crystalline C–S–H are currently underway in our laboratory.

3.3. *Effect of water-to-solid ratio (w/s)*

Water-to-solid ratio (w/s) is one of the most important experimental parameters in hydrothermal syntheses. Effect of w/s was investigated for a sample with fine quartz. Four samples with different w/s were prepared and investigated by in-situ XRD (F-1.7, F-3, F-6 and F-9). Before we describe the in-situ data, we would like to compare the data of last measurement cycle of each sample to show how the final products are different from each other. Fig. 11 shows XRD data of the last measurement cycle for each sample. As described in the previous section, F-1.7 did not show any tobermorite peaks, instead, semi-crystalline C–S–H was observed. All other samples, on the other hand, showed clear tobermorite patterns. Very wide halo ranging from 3 to 13° observed in the F-6 and F-9 patterns is that from water.

The time dependencies of the intensities of each constituent are shown in Fig. 12. Here the time dependence curves of quartz and portlandite are averaged data of several peaks as described in the previous section. Tobermorite peaks showed different time profiles from each other. Among 5 tobermorite peaks, the time profile of T(220) was similar to that of T(400), and the time profile of T(201) was similar to T(222). The peaks that showed similar time profiles are averaged, and plotted in Fig. 12. The vertical

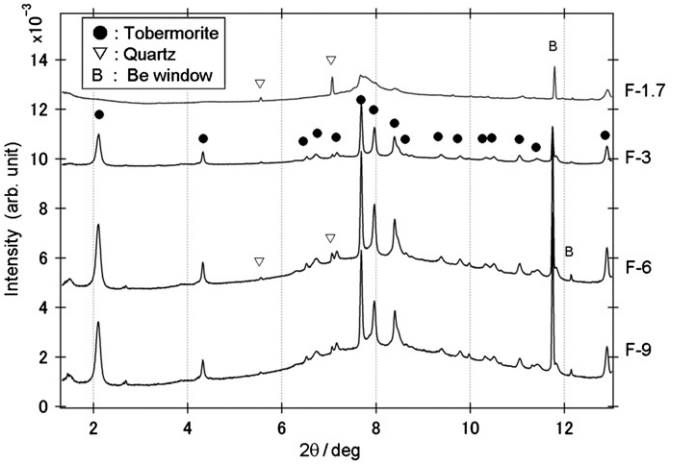

Fig. 11. XRD patterns of the final measurement cycle in in-situ experiment for samples using fine quartz particle with different w/s ratios.

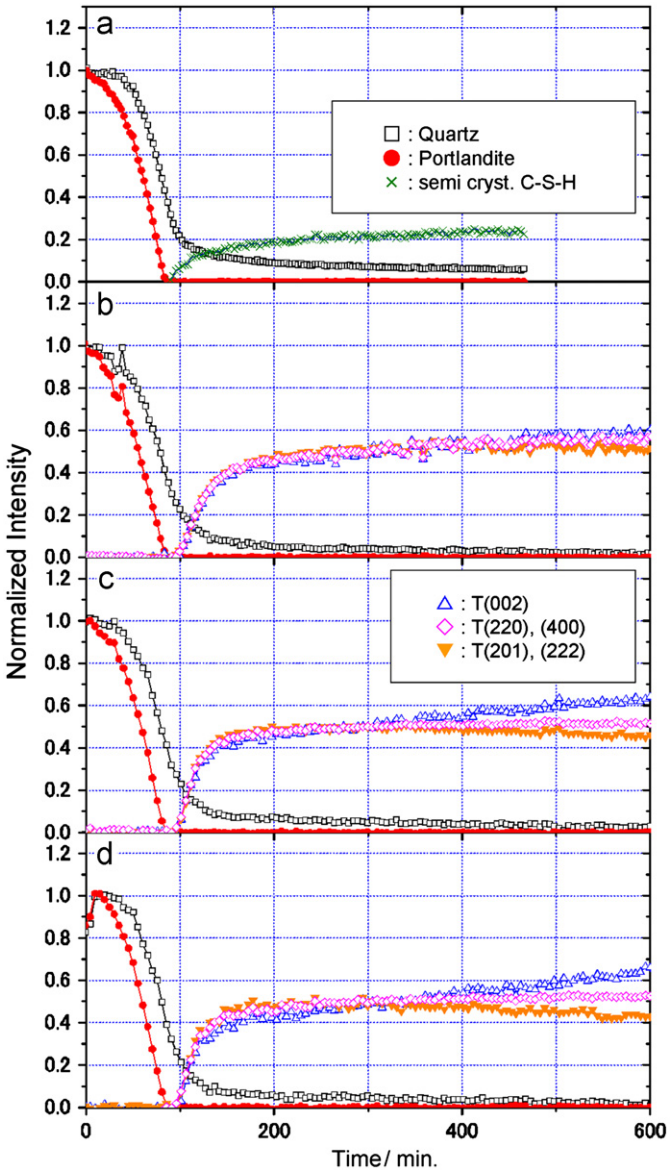

Fig. 12. Time dependence of the averaged peak intensities of the major constituents for (a) F-1.7, (b) F-3, (c) F-6 and (d) F-9.

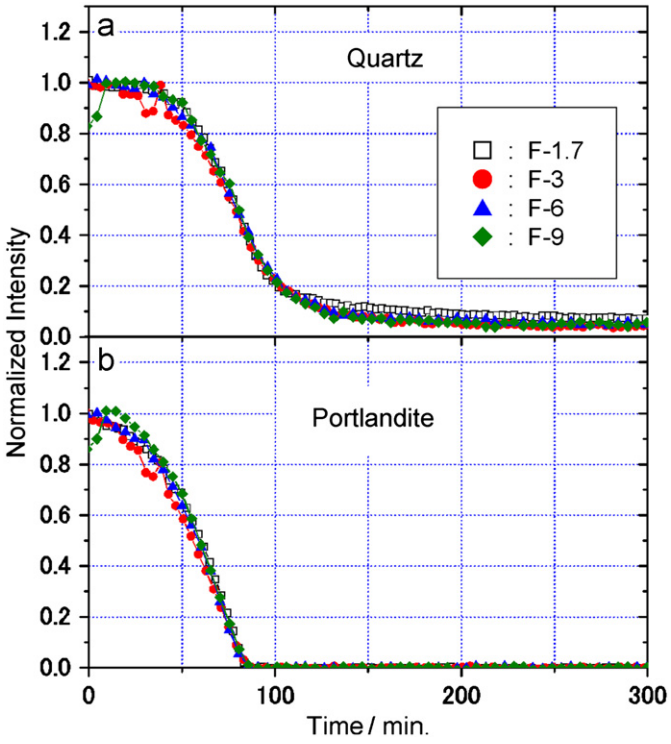

Fig. 13. Overlay plot of time dependence of the averaged peak intensities of (a) quartz and (b) portlandite for samples with different w/s.

scales of three tobermorite curves are normalized so that the initial rises of the profile overlap each other. An overlay plot of the averaged time dependence of quartz and portlandite for four samples is shown in Fig. 13. Surprisingly, quartz dissolution curves of these samples are nearly identical to each other. Even though the water content is largely different by a factor of 5, the dissolution rate does not change at all.

Recently, Houston et. al. [50] reported the effect of w/s on the formation rate of tobermorite using amorphous silica as a starting material. The tobermorite formation rate for a sample with w/s=5 is more than ten times faster than that for a sample with w/s=10. This indicates that the dissolution behavior of fine particle quartz sand under hydrothermal condition is very much different from that of amorphous silica.

The results shown in Fig. 13, together with the results in the previous section, would indicate that the quartz dissolution is governed by its surface area. Also, this indicates that the dissolution rate itself does not affect whether the tobermorite is formed or not in these systems. The curves for portlandite are also nearly

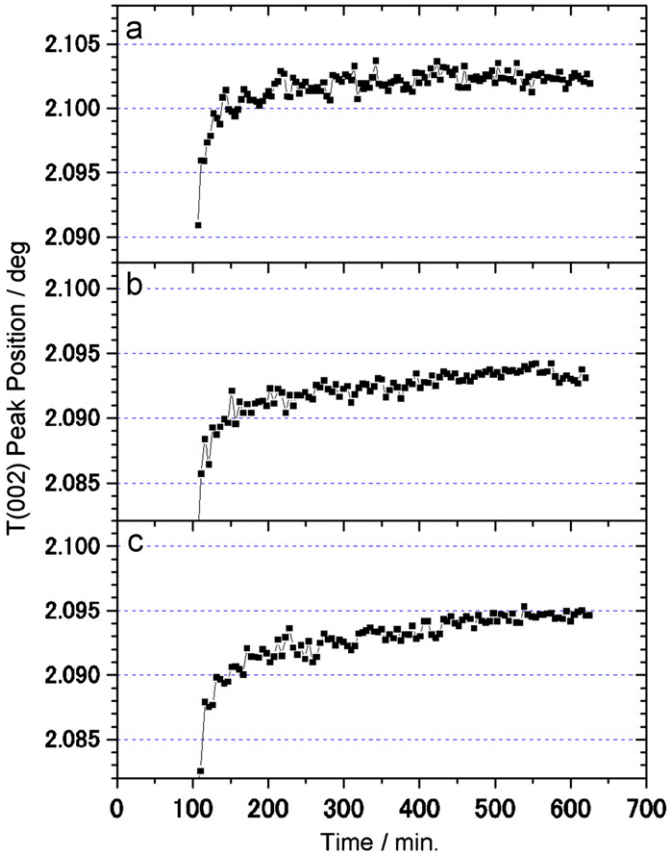

Fig. 14. Time dependences of tobermorite (002) peak positions in (a) F-3, (b) F-6 and (c) F-9.

identical, indicating the dissolution rate of portlandite is largely influenced by that of quartz, as also described in the previous section. The fact that the time dependencies of both quartz and portlandite intensities are identical among these samples implies the Ca/Si ratios of non-crystalline C–S–H are also identical among these samples throughout the reaction. This means the average Ca/Si in non-crystalline C–S–H does not necessarily influence the formation of tobermorite. Rather, concentration of Ca and/or silicate ions in the solution phase would play an important role for tobermorite formation. Mitsuda conducted the measurement of ion concentrations in the solution phase during autoclave for the CaO–quartz–H_2O system with a Ca/Si ratio of 0.8 and water-to-solid ratio of 20 [7]. According to his results, Ca ion concentration during autoclave is close to saturation while silicate ion concentration is about one order of magnitude lower than saturation. This suggests, in the present study, silicate ion concentration in the solution phase is different according to the w/s. It can be assumed that the silicate ion concentration may largely affect the possibility of tobermorite formation. Considering that the structure of semi-crystalline C–S–H is similar to that of tobermorite in ab-plane but without periodic structure along *c*-axis, lower silicate ion concentration in the solution phase would be preferred for formation of the periodic structure along *c*-axis.

It should be noted that the peak intensities of T(002) relative to other tobermorite peaks become larger in the later stages of the autoclave in F-3, F-6 and F-9. This phenomenon is quite similar to that observed in sample C-1.5, as described in the previous section. Peak positions of T(002) during the autoclave are shown in Fig. 14. Slight shift toward high 2θ direction are observed for all samples, implying the chemical composition or structural change during the reaction. Similarly to the case of C-1.5, qualitative trend can be explained by the decrease of interlayer Ca atoms or water molecules. Comparing the time profiles of T(002) in F-3, F-6 and F-9 shown in Fig. 14, the increase of T(002) becomes more remarkable as w/s increases. Lower Ca ion concentration in the solution phase for high w/s samples would lead to the ejection of interlayer Ca from the tobermorite crystal.

Again, detailed structure refinement such as Rietveld analysis will be necessary for further discussion.

4. Conclusions

Hydrothermal formation of tobermorite in simplified model systems was investigated by in-situ XRD. Although the reaction time was largely dependent on the quartz particle size, the average Ca/Si in non-crystalline C–S–H at the timing that either tobermorite or semi-crystalline C–S–H started to be formed (T0) was nearly identical for all samples regardless of the absolute value of T0. The importance of the distribution of the Ca/Si as well as the silicate chain length in non-crystalline C–S–H was suggested. Tobermorite was able to be synthesized with larger w/s, even in fine quartz systems. However, the dissolution curves of both quartz and portlandite are identical among samples with different w/s. It was suggested that lower silicate ion concentration in the solution phase is important for tobermorite formation.

Acknowledgment

This study was performed with the approval of JASRI (Proposal nos. 2009B1788, 2009B2015, 2010A1694 and 2010A1831). Authors are grateful to Dr. Hidenori Toyokawa for his great help for the use of a PILATUS-2M detector.

Appendix A. Supplementary Information

Supplementary data associated with this article can be found in the online version at doi:10.1016/j.jssc.2011.05.061.

References

[1] M.W. Grutzeck, in: M. Scheffler, P. Colombo (Eds.), Cellular Ceramics, Wiley-VCH, Weinheim, 2005, pp. 193–223.
[2] G. Schober, ZKG Int. 58 (2005) 63–70.
[3] J. Alexanderson, Cem. Concr. Res 9 (1979) 507–514.
[4] T. Mitsuda, K. Sasaki, H. Ishida, J. Am. Ceram. Soc. 75 (1992) 1858–1863.
[5] O. Watanabe, K. Kitamura, H. Maenami, H. Ishida, J. Am. Ceram. Soc. 84 (2001) 2318–2322.
[6] H. Sato, M. Grutzeck, Mater. Res. Soc. Symp. Proc. 245 (1992) 235–240.
[7] T. Mitsuda, Ganseki Kobutsu Kosho Gakkaishi 3 (1982) 317–329.
[8] S.A.S. El-Hemaly, T. Mitsuda, H.F.W. Taylor, Cem. Concr. Res 7 (1977) 429–438.
[9] T. Mitsuda, Mineral. J. 6 (1970) 143–158.
[10] G.L. Kalousek, J. Am. Concr. Inst. 26 (1955) 989–1011.
[11] G.L. Kalousek, A.F. Prebus, J. Am. Ceram. Soc. 41 (1958) 124–132.
[12] C.F. Chan, T. Mitsuda, Cem. Concr. Res 8 (1978) 135–138.
[13] K. Luke, Cem. Concr. Res 34 (2004) 1725–1732.
[14] M. Sakiyama, T. Mitsuda, Cem. Concr. Res 7 (1977) 681–686.
[15] E.I. Al-Wakeel, S.A. El-Korashy, J. Mater. Sci 31 (1996) 1909–1913.
[16] T. Mitsuda, H. Toraya, Y. Okada, M. Shimoda, Ceram. Trans. 5 (1989) 206–213.
[17] S. Diamond, J.L. White, W.L. Dolch, Am. Mineral. 51 (1966) 388–401.
[18] S. Komarneni, D.M. Roy, R. Roy, Cem. Concr. Res 12 (1982) 773–780.
[19] G.L. Kalousek, J. Am. Ceram. Soc. 40 (1957) 74–80.
[20] S. Komarneni, R. Roy, D.M. Roy, C.A. Fyfe, C.J. Kennedy, A.A. Bother-By, J. Dadok, A.S. Chesnick, J. Mater. Sci 20 (1985) 4209–4214.
[21] S. Komarneni, M. Tsuji, J. Am. Ceram. Soc. 72 (1989) 1668–1674.
[22] M. Tsuji, S. Komarneni, P. Malla, J. Am. Ceram. Soc. 74 (1991) 274–279.
[23] R. Gabrovšek, B. Kurbus, D. Mueller, W. Wieker, Cem. Concr. Res 23 (1993) 321–328.
[24] P. Norby, A.N. Christensen, J.C. Hanson, Stud. Surface Sci. Catalys. 84 (1994) 179–186.
[25] A.N. Christensen, T.R. Jensen, J.C. Hanson, J. Solid State Chem. 177 (2004) 1944–1951.
[26] T.R. Jensen, A.N. Christensen, J.C. Hanson, Cem. Concr. Res 35 (2005) 2300–2309.
[27] A.C. Jupe, A.P. Wilkinson, K. Luke, G.P. Funkhouser, Ind. Eng. Chem. Res. 44 (2005) 5579–5584.
[28] A.C. Jupe, A.P. Wilkinson, K. Luke, G.P. Funkhouser, Cem. Concr. Res 38 (2008) 660–666.
[29] A.N. Christensen, T.R. Jensen, N.V.Y. Scarlett, I.C. Madsen, J.C. Hanson, J. Am. Ceram. Soc. 87 (2004) 1488–1493.
[30] P. Norby, Curr. Opin. Colloid Interface Sci 11 (2006) 118–125.
[31] D. O'Hare, J.S.O. Evans, R.J. Francis, P.S. Halasyamani, P. Norby, J. Hanson, Micropor. Mesopor. Mat 21 (1998) 253–262.
[32] S. Shaw, S.M. Clark, C.M.B. Henderson, Chem. Geol. 167 (2000) 129–140.
[33] P. Barnes, S.L. Colston, A.C. Jupe, S.D.M. Jacques, M. Attfield, R. Pisulla, S. Morgan, C. Hall, P. Livesey, S. Lunt, in: J. Bensted, P. Barnes (Eds.), Structure and Performance of Cements, second ed.,Spon Press, London, 2002, pp. 477–499.
[34] S.L. Colston, P. Barnes, A.C. Jupe, S.D.M. Jacques, C. Hall, P. Livesey, J. Dransfield, N. Meller, G.C. Maitland, Cem. Concr. Res 35 (2005) 2223–2232.
[35] N. Meller, C. Hall, K. Kyritsis, G. Giriat, Cem. Concr. Res 37 (2007) 823–833.
[36] J. Kikuma, M. Tsunashima, T. Ishikawa, S. Matsuno, A. Ogawa, K. Matsui, M. Sato, J. Synchrotron Radiat. 16 (2009) 683–686.
[37] J. Kikuma, M. Tsunashima, T. Ishikawa, S. Matsuno, A. Ogawa, K. Matsui, M. Sato, J. Am. Ceram. Soc. 93 (2010) 2667–2674.
[38] J. Kikuma, M. Tsunashima, T. Ishikawa, S. Matsuno, A. Ogawa, K. Matsui, M. Sato, Bunseki Kagaku 59 (2010) 489–498.
[39] H.F.W. Taylor, Cement Chemistry, second ed., Thomas Telford, London, 1997, pp. 113–116.
[40] K. Mohan, H.F.W. Taylor, J. Am. Ceram. Soc. 64 (1981) 717–719.
[41] J.L. Larosa-Thompson, M.W. Grutzeck, World Cem. Res. Develop. (1995) 65–71.
[42] Y. Okada, N. Isu, T. Masuda, H. Ishida, J. Ceram. Soc. Jpn. 102 (1994) 1148–1153.
[43] H.F.W. Taylor, Cement Chemistry, second ed., Thomas Telford, London, 1997, pp. 150–156.
[44] C.F. Chan, M. Sakiyama, T. Mitsuda, Cem. Concr. Res 8 (1978) 1–5.
[45] F. Matsushita, Y. Aono, S. Shibata, Cem. Concr. Res 34 (2004) 1251–1257.
[46] K. Inoue, S. Tsunematsu, H. Yamada, Gypsum Lime 229 (1990) 413–418.
[47] O.P. Shrivastava, F.P. Glasser, React. Solids 2 (1986) 261–268.
[48] H.M. Jennings, J. Am. Ceram. Soc. 69 (1986) 614–618.
[49] H.F.W. Taylor, Cement Chemistry, second ed., Thomas Telford, London, 1997, pp. 145–156.
[50] J.R. Houston, R.S. Maxwell, S.A. Carroll, Geochem. Trans. 10 (2009) 1.